Participant and spectator scaling of spectator fragments in Au + Au and Cu + Cu collisions at $\sqrt{s_{NN}} = 19.6$ and 22.4 GeV

B. Alver,[1] B. B. Back,[2] M. D. Baker,[3] M. Ballintijn,[1] D. S. Barton,[3] R. R. Betts,[4] A. A. Bickley,[5] R. Bindel,[5] A. Budzanowski,[6] W. Busza,[1] A. Carroll,[3] Z. Chai,[3] V. Chetluru,[4] M. P. Decowski,[1] E. García,[4] T. Gburek,[6] N. George,[2,3] K. Gulbrandsen,[1] S. Gushue,[3] C. Halliwell,[4] J. Hamblen,[7] I. Harnarine,[4] G. A. Heintzelman,[3] C. Henderson,[1] D. J. Hofman,[4] R. S. Hollis,[4] R. Hołyński,[6] B. Holzman,[3] A. Iordanova,[4] E. Johnson,[7] J. L. Kane,[1] J. Katzy,[1,4] N. Khan,[7] W. Kucewicz,[4] P. Kulinich,[1] C. M. Kuo,[8] W. Li,[1] W. T. Lin,[8] C. Loizides,[1] S. Manly,[7] D. McLeod,[4] A. C. Mignerey,[5] R. Nouicer,[4] A. Olszewski,[6] R. Pak,[3] I. C. Park,[7] H. Pernegger,[1] C. Reed,[1] L. P. Remsberg,[3] M. Reuter,[4] E. Richardson,[5] C. Roland,[1] G. Roland,[1] L. Rosenberg,[1] J. Sagerer,[4] P. Sarin,[1] P. Sawicki,[6] I. Sedykh,[3] W. Skulski,[7] C. E. Smith,[4] M. A. Stankiewicz,[3] P. Steinberg,[3] G. S. F. Stephans,[1] A. Sukhanov,[3] A. Szostak,[3] J.-L. Tang,[8] M. B. Tonjes,[5] A. Trzupek,[6] C. Vale,[1] G. J. van Nieuwenhuizen,[1] S. S. Vaurynovich,[1] R. Verdier,[1] G. I. Veres,[1] P. Walters,[7] E. Wenger,[1] D. Willhelm,[5] F. L. H. Wolfs,[7] B. Wosiek,[6] K. Woźniak,[6] A. H. Wuosmaa,[2] S. Wyngaardt,[3] and B. Wysłouch[1]

(PHOBOS Collaboration)

[1]*Laboratory for Nuclear Science, Massachusetts Institute of Technology, Cambridge, Massachusetts 02139-4307, USA*

[2]*Physics Division, Argonne National Laboratory, Argonne, Illinois 60439-4843, USA*

[3]*Brookhaven National Laboratory, Upton, New York 11973-5000, USA*

[4]*Department of Physics, University of Illinois at Chicago, Chicago, Illinois 60607-7059, USA*

[5]*Department of Chemistry, University of Maryland, College Park, Maryland 20742, USA*

[6]*Institute of Nuclear Physics, Kraków, Poland*

[7]*Department of Physics and Astronomy, University of Rochester, Rochester, New York 14627, USA*

[8]*Department of Physics, National Central University, Chung-Li, Taiwan*

(Received 30 November 2015; published 2 August 2016)

Spectator fragments resulting from relativistic heavy ion collisions, consisting of single protons and neutrons along with groups of stable nuclear fragments up to nitrogen ($Z = 7$), are measured in PHOBOS. These fragments are observed in Au+Au ($\sqrt{s_{NN}} = 19.6$ GeV) and Cu+Cu (22.4 GeV) collisions at high pseudorapidity (η). The dominant multiply-charged fragment is the tightly bound helium (α), with lithium, beryllium, and boron all clearly seen as a function of collision centrality and pseudorapidity. We observe that in Cu+Cu collisions, it becomes much more favorable for the α fragments to be released than lithium. The yields of fragments approximately scale with the number of spectator nucleons, independent of the colliding ion. The shapes of the pseudorapidity distributions of fragments indicate that the average deflection of the fragments away from the beam direction increases for more central collisions. A detailed comparison of the shapes for α and lithium fragments indicates that the centrality dependence of the deflections favors a scaling with the number of participants in the collision.

DOI: 10.1103/PhysRevC.94.024903

I. INTRODUCTION

In relativistic heavy ion collisions, the nucleons of the interacting ions can be divided into two distinct categories: those that experience an inelastic collision with at least one nucleon from the opposing nucleus (participants) and those that do not (spectators). Participant nucleons ultimately create the bulk of particles observed in the detectors. Spectators consist of single protons and neutrons as well as larger spectator fragments including helium, lithium, beryllium, boron, and higher mass nuclei. Naively, these spectators are free to continue along their original path as they do not directly participate in the collision. In practice, however, they can interact in several ways and still be considered a spectator by the usual definition: for example they can suffer an elastic collision with a nucleon from the other beam, they can be affected by any remaining nuclear binding energy in the beam remnant, or they can interact with produced particles from the participant zone [1].

Fragmentation of nuclei has been studied in a number of experiments [2–9]. These experiments typically covered the full kinematic and solid angle range needed to accurately identify all fragments and basic fragment properties such as A and Z, and their momenta. However, these experiments suffered from a lack of statistics, with only $\mathcal{O}(1000)$ events in total, precluding detailed differential studies of fragmentation properties as a function of impact parameter.

The observed properties of fragments, such as their momentum vectors, can be described by a combination of the beam momentum at the time of the collision and the internal Fermi motion within the nucleus in its rest frame. In the absence of Fermi motion and other external effects, spectator fragment transverse momenta would be zero and they would consequently continue traveling at the same rapidity as the beam. In this limit, the polar angle (θ) of fragments would be zero or, equivalently, they would have infinite pseudorapidity (η):

$$\begin{aligned} \eta &= -\ln(\tan(\theta/2)) \\ &\to \infty(\theta \to 0). \end{aligned} \tag{1}$$

Including the Fermi motion, however, leads to a finite transverse momentum component of the fragments and reduces the particle rapidity to below that of the beam. With a finite (nonzero) polar angle, it is possible that the products will

be intercepted by active elements of a detector. In addition, the internal Fermi motion also modifies the longitudinal component of the momentum, however this effect is typically small compared to the boosted momentum of the nucleons.

Transverse momentum is boost invariant and it therefore becomes useful to compare data across multiple experiments with differing collision energies. Equivalently, by converting the momentum vectors into an angular form, one can show that the pseudorapidity density distribution ($dN/d\eta$ versus η) becomes approximately boost invariant, which also allows for the comparison of data at different $\sqrt{s_{NN}}$. To account for energy differences, one subtracts the rapidity of the beam at the appropriate energy scale; a nontrivial transformation described in Appendix A.

In the PHOBOS experiment [10] at the BNL Relativistic Heavy-Ion Collider (RHIC), completely freed neutrons can be measured using the Zero-Degree Calorimeters (ZDCs) [11], which are specifically designed for this purpose. Charged fragments are not observed in these detectors as they are swept away from the ZDCs by the RHIC accelerator magnets. A calorimeter that could detect very forward protons was available for some PHOBOS running periods, but was not used in this analysis. At RHIC injection energies, nucleon-nucleon center of mass energy $\sqrt{s_{NN}} = 19.6$ (Au+Au) and 22.4 GeV (Cu+Cu), spectators with a finite transverse momentum can be detected within the pseudorapidity acceptance of PHOBOS. However, the finite acceptance of the detector limits the measurement of very low-p_T particles, especially for large-Z fragments. A large statistical sample, though, has been amassed which does allow for some more detailed studies not afforded to other experiments.

This paper presents detailed measurements of large-Z fragments in the PHOBOS detector. Section II describes the detector. Section III describes the analysis methods used to distinguish differently charge particles. Sections IV and V show the pseudorapidity and centrality dependencies of the fragments, respectively. Section V B discusses how, in combining the system size, centrality, and pseudorapidity dependencies, one can probe scaling effects of the large-Z fragments in the context of the number of spectators and participants in the collision.

II. PHOBOS DETECTOR

PHOBOS is a large acceptance silicon detector, covering almost 2π in azimuth and $|\eta| < 5.4$ ($\theta > 9$ mrad) [10]. For the results presented here, the energy loss measured in the Ring detectors ($3.0 < |\eta| < 5.4$) is used to identify spectator fragments. The Rings are silicon pad detectors arranged in an octagonal pattern perpendicular to and surrounding the beam pipe. Three Ring detectors are placed on each side of the interaction point at approximately 1, 2, and 5 m from the center of the interaction region. This configuration allows for full coverage with minimal overlapping areas. In addition, the Octagon silicon barrel, which consists of a single-layer of silicon parallel to and surrounding the beam pipe covering $|\eta| < 3.2$, is used for collision vertex and event centrality determination.

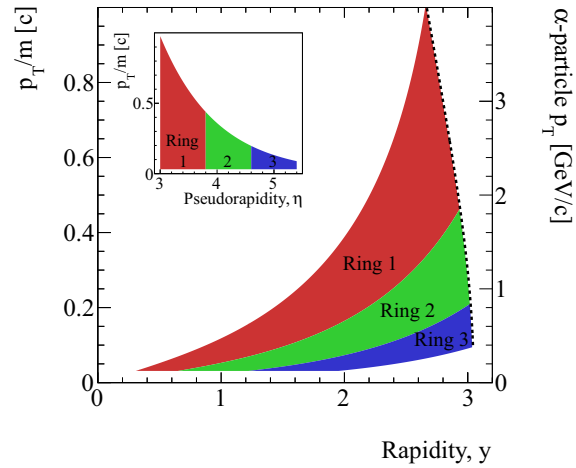

FIG. 1. Transverse momentum and rapidity coverage of charged particles in the silicon Ring detectors in PHOBOS. The main figure shows the p_T/m-rapidity acceptance for charged particles in each Ring (different shaded bands). The boundary on the rightmost edge of the shaded region depends on the beam energy. The dashed line shows the boundary for $p_z/m = p_{\text{beam}}/m_{\text{Au}}$ for $\sqrt{s_{NN}} = 19.6$ GeV Au+Au collisions. The right-hand axis shows the p_T scale for α particles, i.e., $m = 3.727\,\text{GeV}/c^2$. The inset figure shows the Ring-detector p_T and pseudorapidity coverage.

In order to distinguish between singly and multiply charged fragments, the relative energy loss, E_{rel}, is defined as

$$E_{\text{rel}} = \frac{E_{\text{loss}}}{\langle E_{\text{loss}} \rangle|_{Z=1}}, \tag{2}$$

where E_{loss} is the energy loss in the silicon detector and $\langle E_{\text{loss}} \rangle|_{Z=1}$ is the mean energy loss for a $Z = 1$ particle. Singly charged particles (for example spectator protons, deuterons, and tritons) and singly charged participants or produced particles (created by the participants) all appear at an E_{rel} position close to 1 and, as such, cannot be separated. For larger fragments, with charge greater than unity, energy loss in the silicon follows a charge-squared (Z^2) dependence, leading to the appearance of α particles (for example) at four times the E_{rel} position of a singly charged particle.

The transverse momentum, p_T, and rapidity, y, coverage for charged particles in the Rings is shown in Fig. 1. As there is no significant magnetic field traversed by forward-going particles, the fixed η Ring boundaries translate to fixed curves in p_T/m versus y for all charged particles. The high-p_T and y boundary (rightmost edge for each Ring) is calculated for $\sqrt{s_{NN}} = 19.6$ GeV Au+Au collisions, assuming a maximum $p_z/m = p_{\text{beam}}/m_{\text{Au}}$, where p_z is the momentum of the particle (of mass m) along the beam direction, and p_{beam} is the beam momentum.

III. DATA ANALYSIS

A. Event selection

The data were recorded during the 2001 (Au+Au – $\sqrt{s_{NN}} = 19.6$ GeV) and 2005 (Cu+Cu – $\sqrt{s_{NN}} = 22.4$ GeV) RHIC runs. Readout of the silicon was initiated by a minimally biased trigger for each data set based on coinciding signals

from two arrays of 16 plastic scintillators ($3.2 < |\eta| < 4.5$), the "Paddle" trigger counters [12]. For Au+Au (Cu+Cu) collisions, a minimum of three (one) scintillator hits were required in each array to start readout. The collision vertex position along the beam line (z) was determined via a probabilistic approach using hits in the Octagon silicon barrel [13]. For Cu+Cu collisions at $\sqrt{s_{NN}} = 22.4$ GeV, a vertex requirement of $|z| < 10$ cm from the nominal vertex position was imposed; for Au+Au this was relaxed to $|z| < 20$ cm to maximize the statistics from the single day-long run. A total of 8.4×10^3 (2.1×10^6) events were selected for this analysis out of 3.27×10^3 (15.7×10^6) recorded, respectively, for Au+Au (Cu+Cu) collisions. Events are dominantly rejected due to the vertex requirement. The estimated trigger efficiency (coupled with the vertex finding efficiency) for the Au+Au (Cu+Cu) data set is $83.5 \pm 3\%$ ($79 \pm 5\%$), determined using the same methods as described in Ref. [14] with the data divided into seven (six) centrality classes, each with 10% of the total nuclear inelastic cross section. The centrality measure, EOct, is the summed energy loss in the silicon of the centrally located Octagon barrel in the region $|\eta| < 3.0$ [14]. The EOct parameter is defined in a $|\eta|$ region smaller than the full acceptance of the Octagon to limit any systematic effects of acceptance shifts (due to the collision vertex position) and to reduce the overlap with the Ring detector acceptance. The lowest centrality cut-off is defined as the point at which the trigger+vertex efficiency falls below 100%. For each centrality class, the number of participants ($N_{\rm part}$) is estimated by use of a Glauber model calculation [15]. Also, the number of spectator nucleons emitted at either the positive or negative pseudorapidity is calculated as $N_{\rm spec}/2 = (N_{\rm part}^{\rm max} - N_{\rm part})/2$, where $N_{\rm part}^{\rm max} = 2A = 394$ (126) for Au (Cu) nuclei.

B. Motivation

The first observation of the presence of charged spectator fragments, in the acceptance of PHOBOS, was made during the first low-energy data [16]. The measured charged particle multiplicity was found to be larger at high pseudorapidity in peripheral data than in central data, an opposite effect than was expected, and in contrast to the observed dependencies at midrapidity. Several tests were performed to confirm that the larger particle yield at high pseudorapidity likely originated from spectator fragments. Figure 2 shows the correlation between the summed energy in each silicon Ring (ERing) and the summed energy deposited in the silicon Octagon barrel (EOct). Filled symbols represent data; open symbols show the result of a Monte Carlo (MC) simulation that uses particles generated from a HIJING [17] event simulation passed through a full GEANT [18] description of the PHOBOS detector and has had spectator fragments explicitly removed from the acceptance of the detector.

In the MC simulation, a monotonic correlation is observed between ERing 1 and EOct, which becomes weaker for larger pseudorapidities. Even at the highest pseudorapidities, ERing 3 still increases with increasing EOct. In the data, the dependence of ERing 1 on EOct is similar in shape to that found in the MC simulation. At higher pseudorapidities, however, the positive correlation is restricted to the lowest EOct range

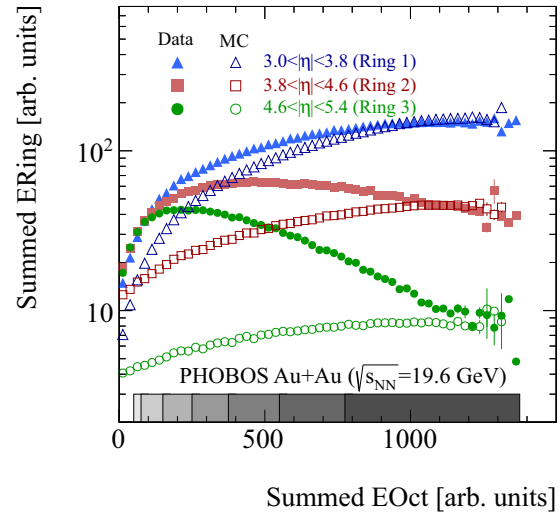

FIG. 2. Correlation between the summed energy recorded in each of the Ring detectors (ERing) and the summed energy deposited in the Octagon barrel (EOct) in Au+Au collisions at $\sqrt{s_{NN}} = 19.6$ GeV. Filled (open) symbols illustrate the measured distributions from data (simulation). Spectators have been explicitly excluded from the simulation distributions. The bands show the centrality class selection bins used in this analysis, with darker bands corresponding to more central events. See text for discussion.

and, after reaching a maximum, ERing 2 and ERing 3 start to decrease with increasing EOct.

This same anticorrelated dependence was observed in Au+Au data at higher energies in the correlation between the Paddle scintillator counters and the ZDCs. The ZDCs detect spectator neutrons and include roughly the same relative η region [i.e., when considering the difference in beam rapidities ($y_{\rm beam}$) for different collision energies: $\eta - y_{\rm beam}$] in $\sqrt{s_{NN}} = 200$ GeV collisions as covered by Rings 2 and 3 for 19.6 GeV, see for example Ref. [19]. It is possible that the multiplicity distribution from produced particles narrows for more central collisions [20], however this could not account for the observed rise/fall behavior.

C. Fragment identification

Fragments are identified using their relative energy loss ($E_{\rm rel}$) in the silicon [see Eq. (2)]. Figure 3 shows the $E_{\rm rel}$ distribution measured in the ERing acceptance for Au+Au collisions at $\sqrt{s_{NN}} = 19.6$ GeV, where no centrality selection is made and only the region $5.0 < |\eta| < 5.4$ is shown in order to make the higher mass fragments more pronounced. In Fig. 3, the data are shown as a blue spectrum along with the distribution expected from singly-charged particles ($Z = 1$, red). The latter is considered to be a "background" to the data and is determined from a MC simulation without spectator fragments. This $Z = 1$ contribution can be explicitly subtracted as it is entirely due to singly charged particles (mostly from the collision) with a typical Landau-like distribution.

D. Subtracting singly charged particles

To determine the spectral shape of the $Z = 1$ contribution, the energy loss signal for single particles is modeled using

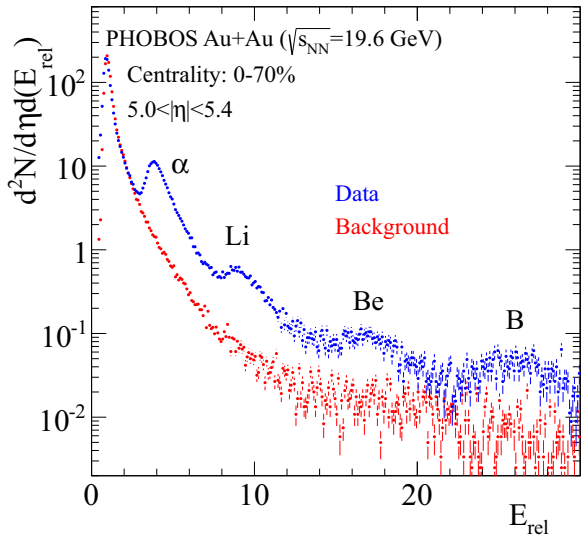

FIG. 3. The distribution of the relative energy loss in Au+Au collisions as $\sqrt{s_{NN}} = 19.6\,\text{GeV}$ averaged over the centrality range 0%–70% and $5.0 < |\eta < 5.4$. The blue distribution shows data, the error bars indicate statistical uncertainties only and the data are not corrected for acceptance. The red distribution shows the results from a MC simulation of singly charged particles with spectator fragments explicitly excluded. See text for discussion.

a full GEANT Monte Carlo (MC) simulation of the PHOBOS apparatus. In data and simulation, it is observed that multiple $Z = 1$ particles can impinge on a single silicon sensor, causing an ensemble distribution over many events to exhibit peaks at $E_{\text{rel}} \sim 2$ and 3 (note that these additional peaks are not clearly visible in Fig. 3). The peak at $E_{\text{rel}} \sim 2$ (which occurs at a rate of about 8% at the highest pseudorapidities) has to be accounted for in the $Z = 1$ subtraction. The third peak is suppressed to a rate of 0.6% and is ignored in this analysis. As this rate is dependent on the charged-particle multiplicity in each detector, this fraction varies with both centrality and pseudorapidity, an effect observed in both data and simulation. Importantly, data with a lesser contribution from a second charged-particle effectively steepens the spectrum, changing the amount of subtracted background.

To account for the second peak in the spectrum, both data and MC are divided into five pseudorapidity and seven (six) centrality classes for the Au+Au (Cu+Cu) analysis, respectively. As the MC distribution only reflects the relative contribution of 1 and 2 singly charged particles, each class produces a spectrum which has a unique shape. To account for the contribution of a second singly charged particle, each data class is systematically compared to all centrality/pseudorapidity classes from the MC, i.e., 35 comparisons, therefore testing the data against a large sample of simulated 2/1 hits-per-sensor contributions. Each MC class is normalized to the data at the first peak (close to $E_{\text{rel}} = 1$ in Fig. 3). The optimal background is chosen as the one with the least χ^2 difference between data and MC E_{rel} spectra, formed over a region around the expected second peak position ($1.5 < E_{\text{rel}} < 2.5$).

To systematically test the sensitivity of the one-to-two hits contribution, $Z = 1$ MC simulation samples with different one-to-two hits ratios are used in the analysis. A systematic uncertainty due to the χ^2 procedure is assigned by considering two further $Z = 1$ distributions. First, the distribution with the next-smallest χ^2 was used, and a full reanalysis was made. Second, a $Z = 1$ distribution with $\chi^2/\text{d.o.f.} = \chi^2_{\text{min}}/\text{d.o.f.} + 1$ was selected, with a full reanalysis performed. A systematic difference of 3%–12% was found for the $Z = 2$ fragment yield in Au+Au collisions in the highest pseudorapidity bins. In pseudorapidity and centrality bins where there is a negligible higher-Z yield, the MC class determined from this analysis closely replicates the entire tail of the singly charged particles.

E. Extracting fragment yields

The measured E_{rel} distribution after subtraction of the fitted $Z = 1$ contribution is shown in Fig. 4(a). The spectrum is dominated by the $Z = 2$ (referred to here as α)[1] fragments. To determine the yield, the peak is fit with a convoluted Landau and Gaussian function (solid red line) in a region close to the α peak, such that the fit range does not overlap the region where the lithium peak is expected. The mean position in the fit is constrained to be the expected mean position for the α fragments. The use of a Landau function is necessary to account for the high tail which partially resides underneath the higher mass peaks—in much the same way that the tail of the singly charged particles contributed to the α peak, before subtraction. The total yield is calculated as the integral of this fit, extrapolated to encompass α fragments appearing at high E_{rel}, for example under the lithium peak (shown by the dashed red line). This extrapolation ultimately contributes less than 10% of the total yield, and the agreement between the raw data and the fit integrated over the same region ($3 < E_{\text{rel}} < 6$) is better than 3%.

The full α contribution to the energy loss spectrum is then subtracted (red line in Fig. 4(a)) to leave only $Z \geqslant 3$ fragments (Fig. 4(b)). Next, with a similar procedure, the yield of lithium fragments is determined using a Landau+Gaussian form (red solid and dashed lines), which is then subtracted from the relative energy loss spectrum. For the final distribution, $Z \geqslant 4$ shown in Fig. 4(c), the effect of the Landau tail is overpowered by the Gaussian width, and thus a two-Gaussian fit is used to extract the yields for beryllium and boron fragments. The mean positions used in this fit are constrained to be the expected position for each fragment. The number of these $Z > 3$ fragments is only 1% of α particles. As such, a small constant offset is allowed to account for possible uncertainties in subtracting α and lithium contributions to the spectrum, which could lead to over- or undersubtraction on the spectrum. For charges greater than five, the full centrality and η dependence is limited by the statistics collected in the single day of Au+Au running at the RHIC injection energy of $\sqrt{s_{NN}} = 19.6\,\text{GeV}$, and are therefore not included in this analysis. The same procedure is used to obtain $Z = 2$ and $Z = 3$ fragment yields in Cu+Cu collisions at $\sqrt{s_{NN}} = 22.4\,\text{GeV}$; $Z > 3$ fragments are not observed, even given the larger statistics of the sample.

[1]Note: $Z = 2$ could imply either ^{3}He or ^{4}He (α). However, as the abundance of ^{4}He is far greater, we refer to $Z = 2$ as α.

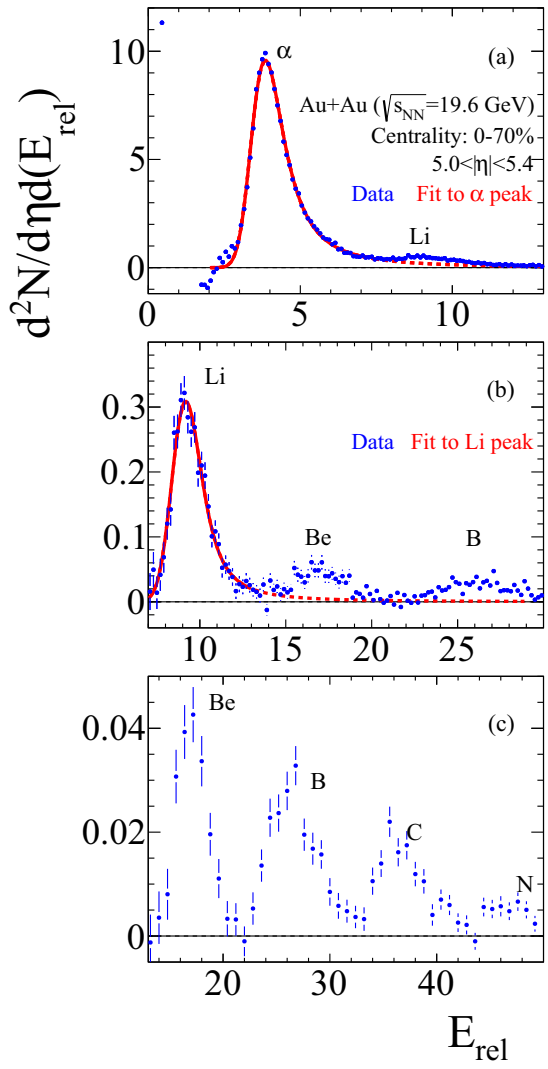

FIG. 4. (a) shows the $E_{\rm rel}$ distribution after subtracting the $Z = 1$ component. The dominant peak at $E_{\rm rel} \sim 4$ corresponds to $Z = 2$ (α) fragments. The red line depicts the fit to determine fragment yields—the solid part shows the region over which the fit was made and the dashed is the extrapolation under the higher-Z peaks. (b) shows the same as (a) but with the contribution from the α spectrum [red line in (a)] removed, highlighting the distribution from $Z \geqslant 3$ fragments. The red line shows a fit to the lithium peak, similar to that described in (a). (c) shows the same as (b), but with the contribution from $Z = 3$ particles removed, and the x axis is extended to show the presence of $Z = 6$ and $Z = 7$ fragments. The error bars are statistical only; data are not corrected for acceptance. See text for discussion.

F. Corrections and systematic uncertainty

The data are corrected for acceptance via simulation which compares the number of tracks which impinge the detectors to all tracks in the full solid angle. As the $Z = 1$ "background" is explicitly subtracted, no further corrections are applied. The effect of absorption of the fragments in the 1 mm thick Beryllium beam pipe was evaluated via a GEANT simulation and was found to be negligible (<1%) as the fragments are high energy—$E_{\rm fragment} \approx 9.8$ GeV (11.2 GeV) per nucleon for Au+Au (Cu+Cu) collisions.

Systematic uncertainties (90% C.L.) are evaluated by performing several checks, in addition to those due to the Landau $Z = 1$ background subtraction. The difference in the extracted yields measured independently in the positive and negative pseudorapidity regions of the PHOBOS detector is found to be 3%–11% for the α yields in Au+Au collisions at the highest pseudorapidities, dependent on centrality. A shift of the measured energy scale in the $E_{\rm rel}$ calculation was applied (±5%) which results in a 1%–8% uncertainty on the α yield for the highest pseudorapidities. A total systematic uncertainty of 11% is assigned on the α yield for the highest pseudorapidities in the 40%–50% centrality class. For larger fragments, an additional uncertainty due to the subtraction of the measured α yield is estimated to be 1.5% for lithium for the highest pseudorapidities in Au+Au collisions. The systematic uncertainties for 40%–50% Au+Au collisions at the highest pseudorapidities are 11%, 20%, and 45% for lithium, beryllium, and boron, respectively.

It was also checked whether fragments could be due to interactions between collision products and the beam pipe, by measuring the number of $Z = 2$ fragments in $\sqrt{s_{NN}} = 62.4$ GeV and 200 GeV data. Few were observed in the former, while none were observed at the highest energy. Should the high-Z fragments have emanated from dead and active detector material, notably the beryllium beam pipe, then the most central $\sqrt{s_{NN}} = 200$ GeV data, which has a larger multiplicity, would have included more background than the lower energy data. Instead, we find no evidence of $Z = 2$ (or higher) fragments in the highest energy data, indicating that such backgrounds from dead material are negligible.

IV. RESULTS I—PSEUDORAPIDITY DEPENDENCE

Both the Au+Au and Cu+Cu data are divided into five bins of pseudorapidity and seven and six bins of centrality, respectively, corresponding to the top 70% (60%) of the nuclear inelastic cross section. Figure 5 shows the measured fragment multiplicity, $dN/d\eta$, as a function of pseudorapidity (tabulated data are included in Appendix C), averaged over both hemispheres (i.e., the number of fragments per colliding nucleus) for Au+Au collisions at $\sqrt{s_{NN}} = 200$ GeV. The first row corresponds to α fragments. Li, Be, and B fragments are shown in subsequent rows. The most central data (those with the least number of spectators after the collision) are shown in the rightmost column; the most peripheral are shown in the leftmost column. As is apparent from this figure, there are no $Z > 1$ fragments for low pseudorapidities ($|\eta| < 4.0$) and only a small number of fragments are produced at high centrality (0%–10% central). The lightest fragment measured (α) is observed in each of the last three $|\eta|$ bins, Lithium fragments are observed in the highest two bins, and beryllium and boron fragments are seen only in the highest $|\eta|$ bin.

Figure 6 shows the measured $dN/d\eta$ for α and lithium fragments in Cu+Cu collisions at $\sqrt{s_{NN}} = 22.4$ GeV—note that lithium yields are scaled up by a factor of 10 for clarity. Similarly to the Au+Au results, no spectator fragments are

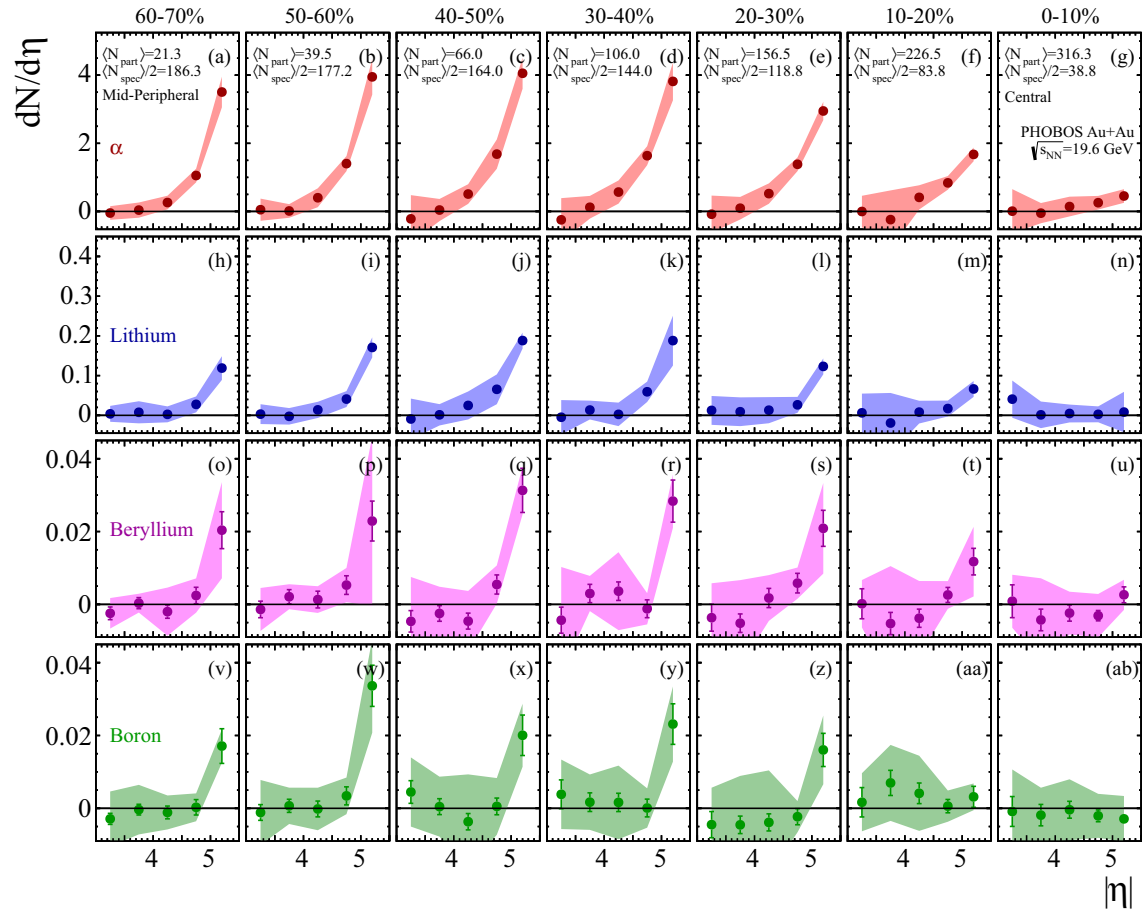

FIG. 5. Pseudorapidity dependence of α [(a)–(g)], lithium [(h)–(n)], beryllium [(o)–(u)], and boron [(v)–(ab)] fragments measured in Au+Au collisions at $\sqrt{s_{NN}} = 19.6$ GeV. Data are presented in bins of centrality (more central in the rightmost panels) and are averaged over both hemispheres, i.e., the number of fragments per colliding nucleus. The error bars represent the statistical uncertainty, the error bands represent 90% C.L. systematic uncertainties in the yield.

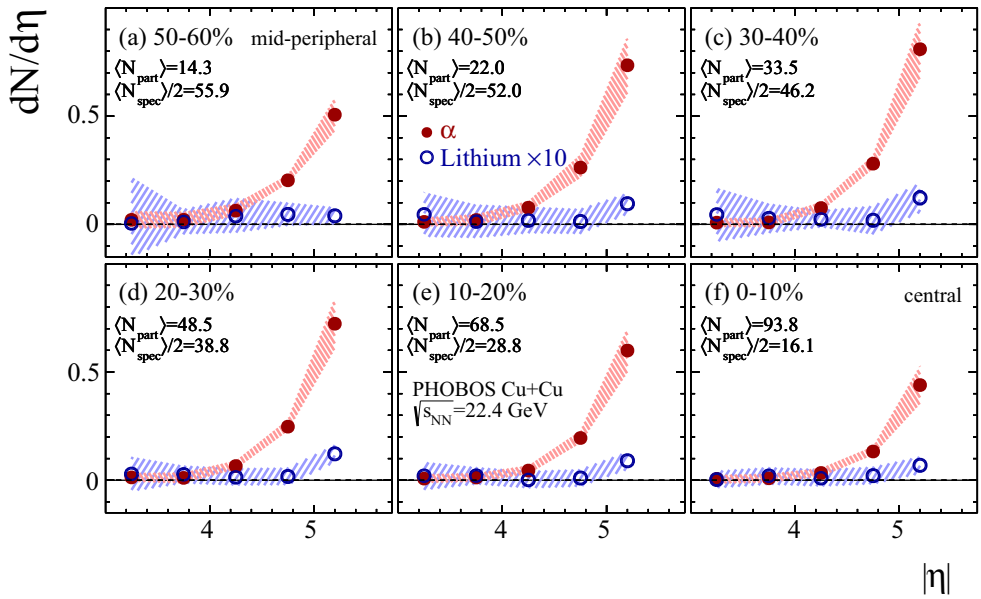

FIG. 6. Pseudorapidity dependence of α (filled symbols) and lithium fragments (open symbols) measured in Cu+Cu collisions at $\sqrt{s_{NN}} = 22.4$ GeV. Lithium fragment yields are scaled up by a factor of 10 for clarity. Data are presented in bins of centrality and are averaged over both hemispheres, i.e., the number of fragments per colliding nucleus. The error bars represent the statistical uncertainty, the error bands represent 90% C.L. systematic uncertainties in the yield.

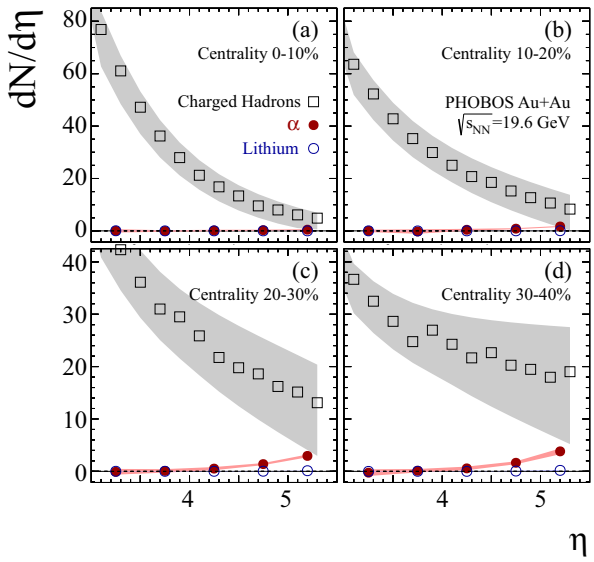

FIG. 7. Comparison between the PHOBOS charged particle multiplicity measured at positive η in Au+Au collisions at $\sqrt{s_{NN}} = 19.6\,\text{GeV}$ and the yield of α and lithium fragments, averaged over positive and negative $|\eta|$. (a), (b), (c), and (d) show the distributions in centrality bins 0%–10%, 10%–20%, 20%–30%, and 30%–40%, respectively. The open squares/light grey bands represents the PHOBOS multiplicity [20], filled (open) circles represent the measured α (Li) yields.

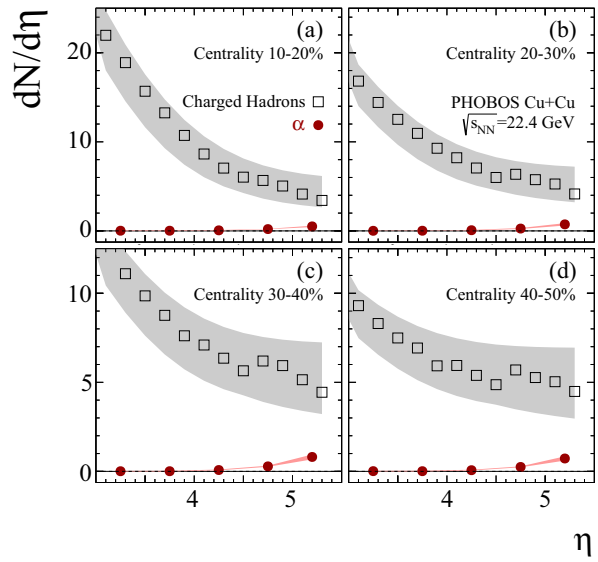

FIG. 8. Comparison between the measured PHOBOS charged particle multiplicity in Cu+Cu collisions at $\sqrt{s_{NN}} = 22.4\,\text{GeV}$ and the yield of α fragments. (a), (b), (c), and (d) show the distributions in centrality bins 10%–20%, 20%–30%, 30%–40%, and 40%–50%, respectively. The open squares/light grey bands represents the PHOBOS multiplicity [20], filled circles represent the measured α yields.

observed in the low pseudorapidity region; lithium fragments are only observed in the highest pseudorapidity bins.

A. Comparison to charged-particle pseudorapidity density

PHOBOS has measured charged particle production in the very forward region ($|\eta| >\sim 3$) for Au+Au and Cu+Cu collisions [16,20,21]. It was observed that the yield of charged particles in this forward pseudorapidity region is larger in the most peripheral collisions compared to the central ones. In those analyses, both singly and multiply charged particles would have been counted as one "charged particle", so it was unclear how many of these particles were protons (or deuterons or tritons) and how many were multiply charged fragments. Figure 7 and 8 shows a comparison between the pseudorapidity-averaged α yield in Au+Au (Cu+Cu) collisions measured in this analysis and the charged-particle multiplicity ($\eta > 3$) from the prior PHOBOS analyses [20]. For these centrality bins, the yield of multiply charged spectator fragments for both systems is typically small ($dN_\alpha/\text{d}\eta = 3.8 \pm 0.6$ in 30%–40% central collisions at $\sqrt{s_{NN}} = 19.6\,\text{GeV}$) compared to the total charged-particle multiplicity ($18.5\,^{+9.2}_{-12.5}$). Therefore, the majority of the particles in the forward region included in the previously published analyses are singly-charged. Averaged over centrality, the small abundance of multiply charged relative to singly-charged particles at the highest pseudorapidity is also clearly seen in Fig. 3. While the relative amount of multiply charged spectators is small, their existence within the detector acceptance confirms our original assertion that the multiplicity at large pseudorapidity is influenced by spectators.

B. Comparison to other fragment data

The number of α particles measured by PHOBOS is found to be similar to the yields measured in other experiments. Figure 9 compares the measured $dN_\alpha/d\eta$ from PHOBOS

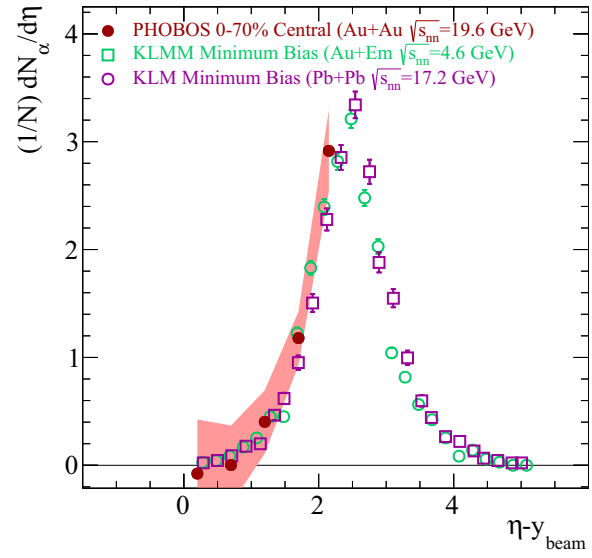

FIG. 9. Comparison of α yields between PHOBOS data from Au+Au collisions ($\sqrt{s_{NN}} = 19.6\,\text{GeV}$) and Au+Em ($\sqrt{s_{NN}} = 4.6\,\text{GeV}$) [4] and Pb+Pb ($\sqrt{s_{NN}} = 17.2\,\text{GeV}$) [7] collisions. PHOBOS data are averaged over positive and negative η and over the most central 0%–70% cross section (filled circles and shaded band which represent the 90% C.L. systematic uncertainties in the yield) for α particles. The pseudorapidity (x axis) is relative to the rest frame of the target nucleus for each energy, as discussed in Appendix A.

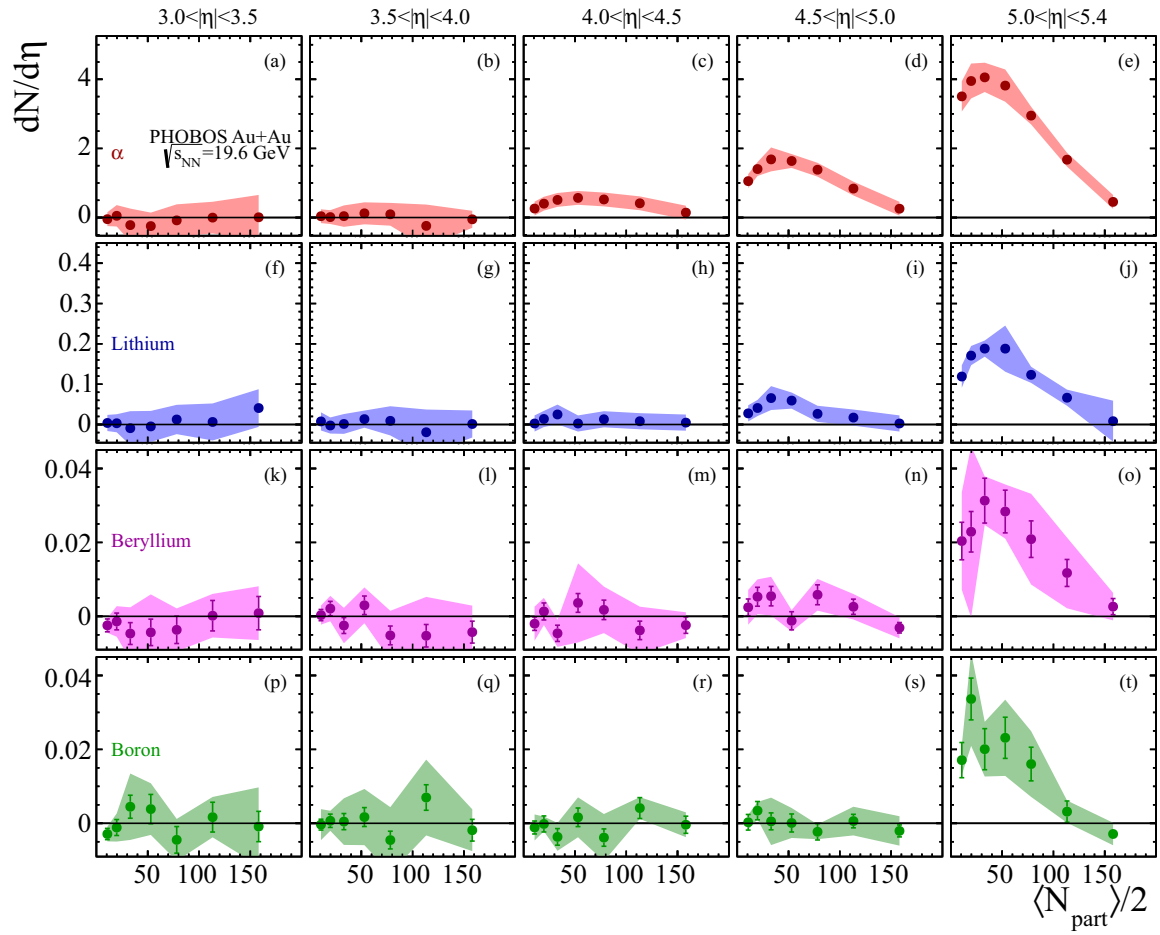

FIG. 10. Centrality dependence of α [(a)–(e)], lithium [(f)–(j)], beryllium [(k)–(o)], and boron [(p)–(t)] fragments measured in Au+Au collisions at $\sqrt{s_{NN}} = 19.6$ GeV. Data are presented in bins of pseudorapidity, η, with the lowest η shown in the leftmost panels. The data are averaged over both hemispheres, i.e., the number of fragments per colliding nucleus. The error bars represent the statistical uncertainty, the error bands represent 90% C.L. systematic uncertainties in the yield. The errors associated with the centrality variables (here $N_{\text{part}}/2$) are not shown on the figures, see Tables II–VII.

(filled circles with a band representing the 90% C.L. systematic uncertainties in the yield) with that from the KLMM [4] [Au projectile with beam energy 10.6 GeV per nucleon on a fixed emulsion (Em) target] and KLM [7] (Pb projectile with beam energy 158 GeV per nucleon on a fixed Pb target) collaborations.[2] Note that the PHOBOS data are effectively a collision of a Au projectile with $E_{\text{beam}} = 9.8$ GeV per nucleon on a target Au nucleus (albeit moving) where this energy is that of a single beam in the collider, i.e., $\sqrt{s_{NN}}/2$. The data are shifted along the x axis in Fig. 9 by the corresponding beam rapidity in each case. A detailed discussion of the properties of this shifted variable ($\eta' = \eta - y_{\text{beam}}$ or for symmetric collisions $\eta' = |\eta| - y_{\text{beam}}$) is given in Appendix A. Any impact of the difference of collision energy should be fully compensated by this beam rapidity shift, however as neither the collision systems nor the event selection are identical some systematic differences are expected. Small differences in yield between Au+Au and Pb+Pb might arise from the fact that the Pb+Pb collisions from the KLM analysis are on average more peripheral (covering 0%–100%) than the Au+Au collisions (0%–70%) from this analysis. As such, any excess yield in the PHOBOS measurements might be due to the missing 30% of the most peripheral events in this data set. Moreover, we do not see any additional systematic effect between our data and the KLMM data that collided Au nuclei on Em (comprising much smaller nuclei: H, He, C, Ag, and Br).

Although a large part of the α yield is outside the acceptance of PHOBOS, the yield in the measured region agrees reasonably well between experiments, and also illustrates the relevance of limiting fragmentation for spectators [16]. While Appendix A carefully describes why beam rapidity is an appropriate scale to shift data at different energies, it is more intuitive to compare boost-invariant quantities such as dN/dp_T. Appendix B estimates a conversion of the presented data into dN/dp_T as a function of p_T, and compares the resulting distributions with those estimated from lower energy collisions, see Fig. 18. From the Appendix, one can see that the lowest transverse momentum particles are not measured

[2]The error bars shown for KLM and KLMM data in Fig. 9 are based on the number of counts, N, in each η bin as $\sqrt{N}$.

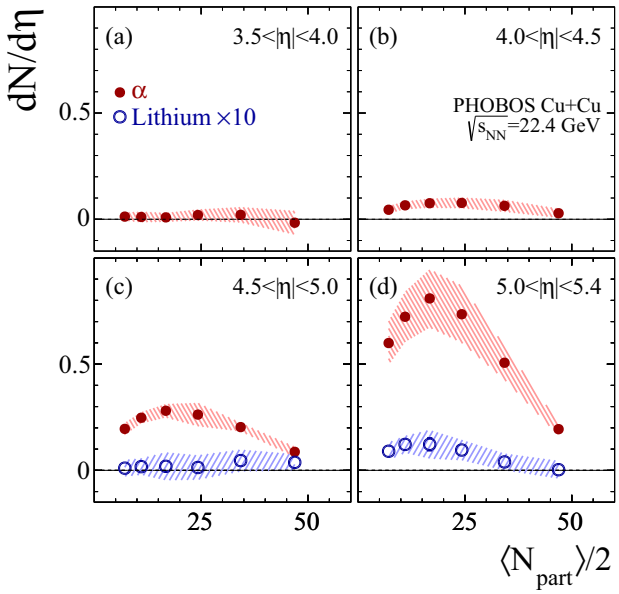

FIG. 11. Centrality dependence of α fragments (filled symbols) for $\sqrt{s_{NN}} = 22.4$ GeV Cu+Cu collisions for four $|\eta|$ bins [(a)–(d)]. For clarity, lithium (open symbols) are scaled up by a factor of 10 and are only shown for the highest two pseudorapidity bins [(c) and (d)]. The data are averaged over both hemispheres, i.e., the number of fragments per colliding nucleus. The error bars (typically smaller than the symbol height) represent the statistical uncertainty, the error bands represent 90% C.L. systematic uncertainties in the yield.

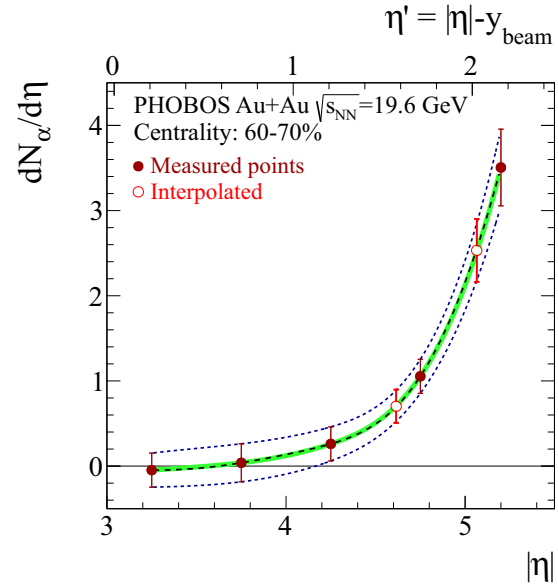

FIG. 12. Spline polynomial fits (lines) to α yields from Au+Au peripheral (60%–70%) data (filled circles). Interpolated points at $\eta' = 1.57$ and $\eta' = 2.02$ are shown as open circles. The scale on the upper x axis shows $\eta' \equiv |\eta| - y_{\rm beam}$. The dashed and green lines show fits using polynomials of different order. The outer dotted lines represent a fit to points at the extreme of the systematic uncertainty bands.

within the PHOBOS acceptance, see Fig. 18. This does not overtly influence the comparison between our data and that from other experiments as the lowest-p_T are predominantly at higher pseudorapidities for spectator fragments (see Fig. 1 and discussion).

The Cu+Cu data are not shown as the expected difference in yield between Au (197) fragments and Cu (63) fragments is large because of the difference in mass—whereas the difference between Au (197) and Pb (208) should be negligible.

V. RESULTS II—CENTRALITY DEPENDENCE

Another way to look at this data is to examine the centrality dependence, shown in Fig. 10 for Au+Au collisions at $\sqrt{s_{NN}} = 19.6$ GeV. Here, the absence of fragments at low pseudorapidity is highlighted in the first two columns. Each $|\eta|$ bin with a significant signal (panels c–e, i, j, o, t) shows a similar pattern: an increase of the yield for peripheral events, a turn-over for midcentral events, and finally an almost linear decrease with $N_{\rm part}/2$ toward the fully overlapping collisions. A similar dependence is also seen in the measured ZDC energy distribution versus centrality in the peripheral region at very high pseudorapidity, see for example Ref. [22].

In Cu+Cu collisions at $\sqrt{s_{NN}} = 22.4$ GeV, a similar centrality dependence is observed for α and lithium fragments in Fig. 11.

A. Comparison of Au+Au and Cu+Cu data

It should be noted that the relative coverage ($\eta' \equiv |\eta| - y_{\rm beam}$) of the detector is not quite the same for Au+Au and Cu+Cu collisions owing to the different beam rapidities: $y_{\rm beam} = 3.04$ (3.18) for Au+Au (Cu+Cu). Therefore, in comparing the two data sets, data points are evaluated at the same average η', via an interpolation between measured points.

To evaluate the yield at each η', a polynomial spline fit is made which smoothly connects the measured data points. The uncertainty in this method is evaluated with two different fits, which are found to be within 10% of the associated data point systematic uncertainty. Figure 12 shows an example of a fit to peripheral (60%–70%) Au+Au ($dN_\alpha/d\eta$) data to determine interpolated points at $\eta' = 1.57$ and $\eta' = 2.02$. A similar fit is made to Cu+Cu data to determine an interpolated point at $\eta' = 1.21$.

A comparison of the centrality dependence of α and lithium yields for Au+Au and Cu+Cu is given in Fig. 13. The data are averaged over both hemispheres, representing the fragments from a single gold (or copper) nucleus. The yield of α and lithium fragments are shown versus $N_{\rm spec}/2$ from a single nucleus. Note that the x axis is inverted such that central collisions are located rightmost on the figure. The magnitude of the yields of fragments is proportional to $N_{\rm spec}/2$ over a wide range of number of spectators. This behavior provides a simple explanation for the smaller number of fragments observed in peripheral Cu+Cu collisions compared to those from peripheral Au fragmentation. Modulo the drop-off for the most peripheral collisions, yields are approximately similar in the two systems for similar $N_{\rm spec}/2$.

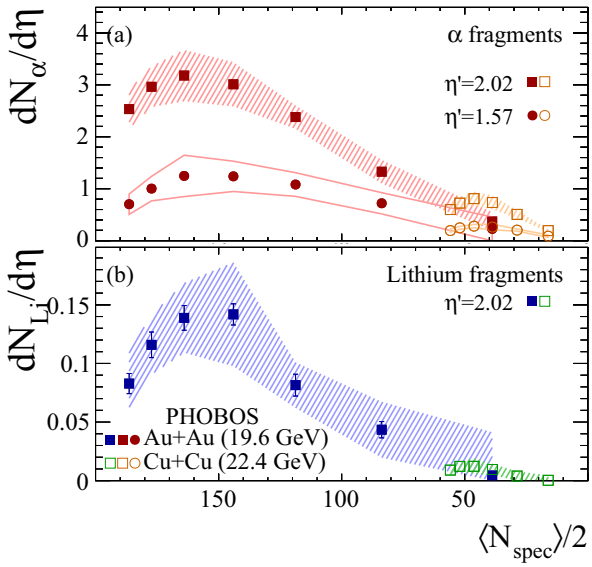

FIG. 13. Centrality dependence of α (a) and lithium yields (b) in $\sqrt{s_{NN}} = 19.6$ GeV Au+Au (filled symbols) and 22.4 GeV Cu+Cu (open symbols) collisions. Note that the centrality variable is not $N_{\rm part}/2$ but $N_{\rm spec}$ from a single nucleus—see text for details—and the x axis runs backwards, central collisions are the rightmost data points. The α data are evaluated at $\eta' = 1.57$ (circles/unfilled systematic bands) and $\eta' = 2.02$ (squares/filled systematic bands). Lithium yields are only shown for $\eta' = 2.02$. The bands represent 90% C.L. systematic uncertainties in the yield.

There is some evidence that, at the same $N_{\rm spec}/2$, the yield of α fragments is higher in Cu+Cu than in Au+Au, which is not apparent for lithium. This is possibly due to a preference for emitting smaller fragments in the smaller copper nucleus.

B. Pseudorapidity and centrality dependence of yields

The simultaneous pseudorapidity and centrality dependencies of the yields can be explored by use of ratios of data, to investigate whether the fragments appear at the same relative position for all centralities or not. Figure 14 shows the ratio of the yield of Li to He fragments evaluated at $\eta' = 2.02$. The three panels show the same data as a function of (a) $N_{\rm spec}/2$, (b) $N_{\rm part}/2$, and (c) the collision geometry ($N_{\rm spec}/2A$). Between Au+Au and Cu+Cu collisions, the Li/α ratios clearly do not exhibit a scaling with either $N_{\rm part}/2$ (i.e., a similar Li/α ratio at a similar $N_{\rm part}/2$) or with collision geometry. The collision geometry, defined as $N_{\rm spec}/2A$, represents the fraction of total nuclear volume which interacts such that the overlap shape for each nucleus is roughly similar. A scaling with $N_{\rm spec}/2$ is suggested by the data—the decreased ratio would indicate that the emission of the lighter fragments is favored for fewer spectator nucleons from the collision system. However, the possibility that this ratio for each system is constant with centrality is not ruled out within the systematic uncertainty. For this scenario, the lower Cu+Cu ratio would indicate a more favorable emission of the lighter fragment in the Cu+Cu system than in Au+Au collisions.

From this data, one may attempt to draw a picture of the emission process for fragments. Unless the spectator nucleons acquire some p_T from intrinsic Fermi motion or the collision process itself, they would simply travel straight down the beam pipe until the magnetic field of the RHIC steering magnets bent them away. In such a case, they would not be visible in the detector as these magnets are located too far from the apparatus to have had any influence on the fragments. The movement of the fragments must be connected to the nucleus and/or be the result of the collision.

In the simplest scenario, the fragments would move outward due to their intrinsic (precollision) motion, without further interaction. This, however, would result in the centrality and pseudorapidity dependencies being decoupled from each other. Specifically, the data in every pseudorapidity interval should have the same centrality dependence (although with different yields); this is not seen in the data. Figures 15 and 16 show the ratio of α yields evaluated at $\eta' = 1.57$ and $\eta' = 1.21$, respectively, divided by the yield at $\eta' = 2.02$, for both Au+Au and Cu+Cu collision systems. The three panels show the same data as a function of (a) $N_{\rm spec}/2$, (b) $N_{\rm part}/2$, and (c) the collision geometry.

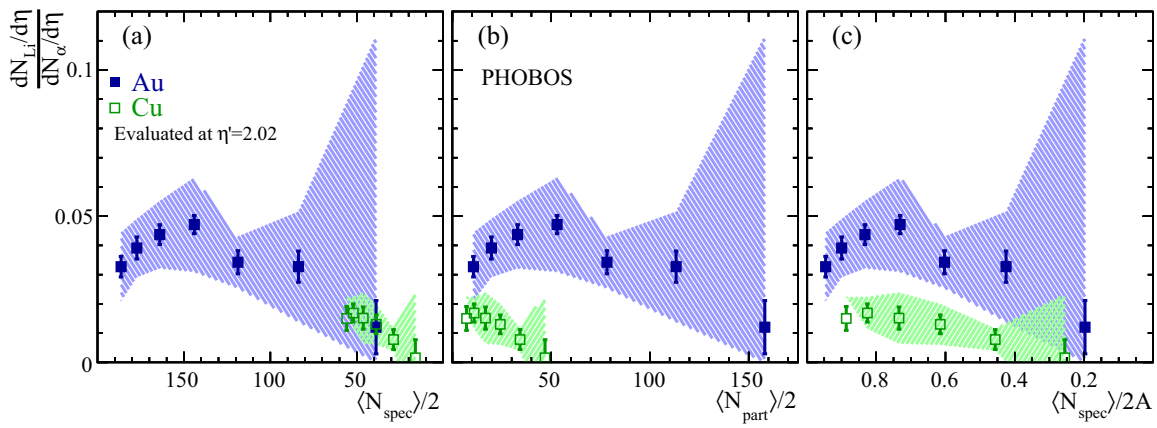

FIG. 14. Centrality dependence of the yield of lithium nuclei divided by that of α particles evaluated at $\eta' = 2.02$. Au+Au (filled symbols) and Cu+Cu (open symbols) collision data are shown as a function of (a) $N_{\rm spec}/2$, (b) $N_{\rm part}/2$, and (c) the collision geometry ($N_{\rm spec}/2A$). The bands represent 90% C.L. systematic uncertainties in the ratio.

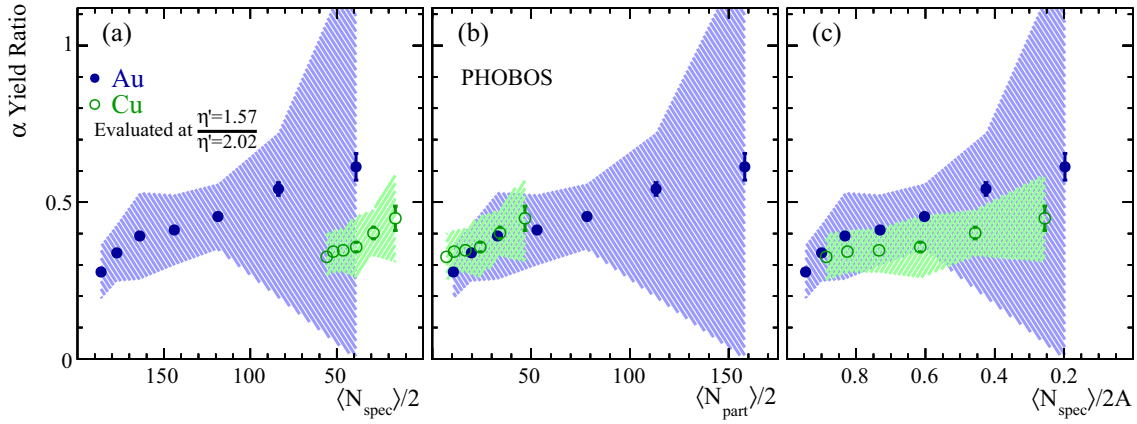

FIG. 15. Centrality dependence of the yield of α particles evaluated at $\eta' = 1.57$ divided by the yield measured at $\eta' = 2.02$. Au+Au (filled symbols) and Cu+Cu (open symbols) collision data are shown as a function of (a) $N_{\rm spec}/2$, (b) $N_{\rm part}/2$, and (c) the collision geometry ($N_{\rm spec}/2A$). The bands represent 90% C.L. systematic uncertainties in the ratio.

The ratios in Figs. 15 and 16 are not constant as the number of α particles in each η' range ($\eta' = 1.57$ and 1.21, respectively) diminishes (compared to the reference at $\eta' = 2.02$) with decreasing centrality. Effectively, the α particles are moving out of the acceptance of the detector for more peripheral collisions and the average deflection away from the beam direction increases for more central collisions. Such a deflection is suggestive of a specific dependence of transverse momentum acquired by the fragments. The same effect is also observed in Cu+Cu collisions. For fragments moved into the acceptance of PHOBOS due to intrinsic (precollision) motion, one would expect no centrality dependence of these ratios, i.e., all flat. Comparing the Cu+Cu and Au+Au data in the three scaling scenarios, it is apparent that these ratios favor a scaling with $N_{\rm part}/2$, which is perhaps counterintuitive as these spectators are often considered to be independent of interactions in the hot participant zone.

VI. CONCLUSION

In conclusion, nuclear fragments ($Z > 1$) have been observed up to $Z = 7$ using the extensive reach in pseudorapidity of the PHOBOS detector. The pseudorapidity and centrality dependence is shown for fragments up to $Z = 5$ only for Au+Au; for Cu+Cu this study is restricted to $Z = 2$ and 3. Fragments from Au+Au ($\sqrt{s_{NN}} = 19.6$ GeV) and Cu+Cu ($\sqrt{s_{NN}} = 22.4$ GeV) collisions have sufficiently low longitudinal momentum that even fragments which have a modest p_T are deflected into the PHOBOS apparatus. The observed rise in charged-particle multiplicity at large pseudorapidity for more peripheral compared to central collisions is observed to be dominated by singly charged particles. However, the existence of large fragments within the detector acceptance confirms our assertion that the multiplicity at large pseudorapidity is influenced by spectators. The yield of α fragments is observed to be similar to that measured in other experiments over a range

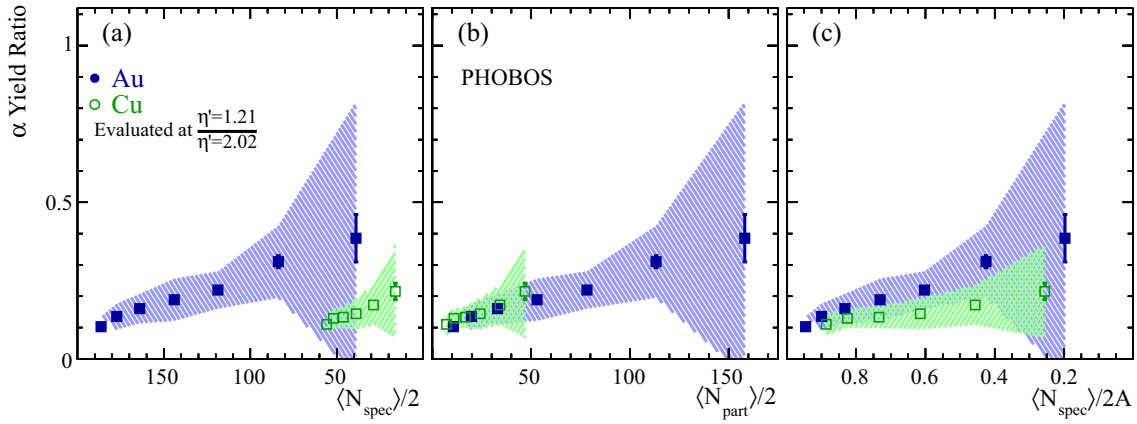

FIG. 16. Centrality dependence of the yield of α particles evaluated at $\eta' = 1.21$ divided by the yield measured at $\eta' = 2.02$. Au+Au (filled symbols) and Cu+Cu (open symbols) collision data are shown as a function of (a) $N_{\rm spec}/2$, (b) $N_{\rm part}/2$, and (c) the collision geometry ($N_{\rm spec}/2A$). The bands represent 90% C.L. systematic uncertainties in the ratio.

of energies if evaluated at the same value of $\eta - y_{\rm beam}$. As a function of centrality, the yield of α and lithium fragments is found to approximately scale with the number of spectators in the collision. The centrality dependence of ratios of α fragment yields at different pseudorapidities illustrates that these fragments move out of the acceptance of the detector for more peripheral collisions. In comparing Cu+Cu and Au+Au ratios, a scaling with the number of participants is favored, suggesting an influence of the hot participant zone with the nonparticipating spectators.

ACKNOWLEDGMENTS

This work was partially supported by U.S. DOE grants no. DE-AC02-98CH10886, DE-FG02-93ER40802, DE-FG02-94ER40818, DE-FG02-94ER40865, DE-FG02-99ER41099, and DE-AC02-06CH11357, by U.S. NSF grants no. 9603486, 0072204, and 0245011, by Polish National Science Center grant no. DEC-2013/08/M/ST2/00320, by NSC of Taiwan Contract NSC 89-2112-M-008-024, and by Hungarian OTKA grant (no. F 049823).

APPENDIX A: RELATING Y AND η

Rapidity, y, is defined in Eq. (A1) from Ref. [23] and has a simple one-to-one relationship with the longitudinal velocity, β_z:

$$y \equiv \frac{1}{2}\ln\left(\frac{E+p_z}{E-p_z}\right) = \tanh^{-1}\left(\frac{p_z}{E}\right) = \tanh^{-1}\beta_z, \quad \text{(A1)}$$

where E is the total energy of the particle and p_z is the longitudinal momentum, i.e., the component along the beam direction. In addition, rapidity has the well-known property that longitudinal boosts are simply additive, where rapidity differences, $y_1 - y_2$, are invariant under longitudinal boosts.

In some cases, such as in the PHOBOS multiplicity detector, only a particle's direction (θ—polar angle and ϕ—azimuthal angle) is accessible, and not the actual momentum. In such cases we use the pseudorapidity variable, η—Eq. (A2), from Ref. [23]:

$$\eta \equiv -\ln(\tan(\theta/2)), \quad \text{(A2)}$$

where θ is the polar angle with respect to the beam direction. In order to relate these two quantities, one can use two identities from Ref. [23]:

$$p_z = m_T \sinh y, \quad \text{(A3)}$$

where m_T is the transverse mass, defined as $m_T^2 = m^2 + p_T^2$, and

$$p_z = p_T \sinh\eta, \quad \text{(A4)}$$

which can be derived from

$$\sinh\eta = \cot\theta. \quad \text{(A5)}$$

These identities result in the relation:

$$\sinh\eta = (\sinh y)\sqrt{1+\frac{m^2}{p_T^2}}. \quad \text{(A6)}$$

1. Mapping η' to y' versus p_T/m

The resulting relation between y and η [Eq. (A6)] has many implications:

(1) $\eta/y \geqslant 1$, which leads directly to
(2) y and η have the same sign, and
(3) $|\eta| > |y|$.

One can examine two limits of this relation. First, in the limit of small η (and therefore also small y), $\sinh\eta \to \eta$ and therefore

$$\eta \approx y\sqrt{1+\frac{m^2}{p_T^2}}. \quad \text{(A7)}$$

Second, and more importantly for this work, at large y (and therefore also large η) one can write

$$\sinh y = e^y(1-e^{-2y})/2 \to e^y/2. \quad \text{(A8)}$$

Using Eq. (A6) this leads to

$$\eta \approx y + \frac{1}{2}\ln\left(1+\frac{m^2}{p_T^2}\right). \quad \text{(A9)}$$

Finally, using the definitions: $\eta' \equiv \eta - y_{\rm beam}$ and $y' \equiv y - y_{\rm beam}$:

$$\eta' \approx y' + \frac{1}{2}\ln\left(1+\frac{m^2}{p_T^2}\right). \quad \text{(A10)}$$

Equation (A10) holds the key information in the relations between y' and η': at large y, an η' bin corresponds to a fixed region in $(y', p_T/m)$ space, independent of $y_{\rm beam}$. Therefore, this formulation represents the best way to compare $dN/d\eta$ distributions measured at various beam energies.

One can estimate the validity of this approximation by calculating the absolute error at each rapidity. An upper bound on the absolute error from Eq. (A10) is given by $|\ln(1-e^{-2y})| \approx e^{-2y}$. For $y > 2 (> 3, > 5)$, the error is estimated to be less than 0.02 ($<2.5\times10^{-3}$, $<5.0\times10^{-5}$) units. Even for $y = 1$, the error in the "large-y" approximation is less than 0.145.

To further illustrate this approximation, for a fixed window in η' ($1.8 < \eta' < 2.0$), Fig. 17 shows the y'-p_T/m acceptance. Panels (a–c) show bands representing the different beam energies used in this paper: (a) $\sqrt{s_{NN}} = 19.6$ GeV, and 22.4 GeV representing Au+Au and Cu+Cu collision data, respectively, measured by PHOBOS, (b) $E_{\rm beam} = 10.6$ GeV collisions of Au nuclei on an emulsion target (Em) measured by KLMM, and (c) $E_{\rm beam} = 158$ GeV collisions of Pb nuclei on a stationary Pb target as measured by KLM. Panel (d) shows an overlay of all distributions. The arrows represent midrapidity (i.e., $y = 0$ and $\eta = 0$). The three lowest energy bands (PHOBOS and KLMM) almost entirely overlap owing to their very similar beam energies (or equivalently $y_{\rm beam}$).

In general, to compare results in the rest frame of the beam particle, PHOBOS has used η' to compare pseudorapidity distributions in the "fragmentation" or "extended

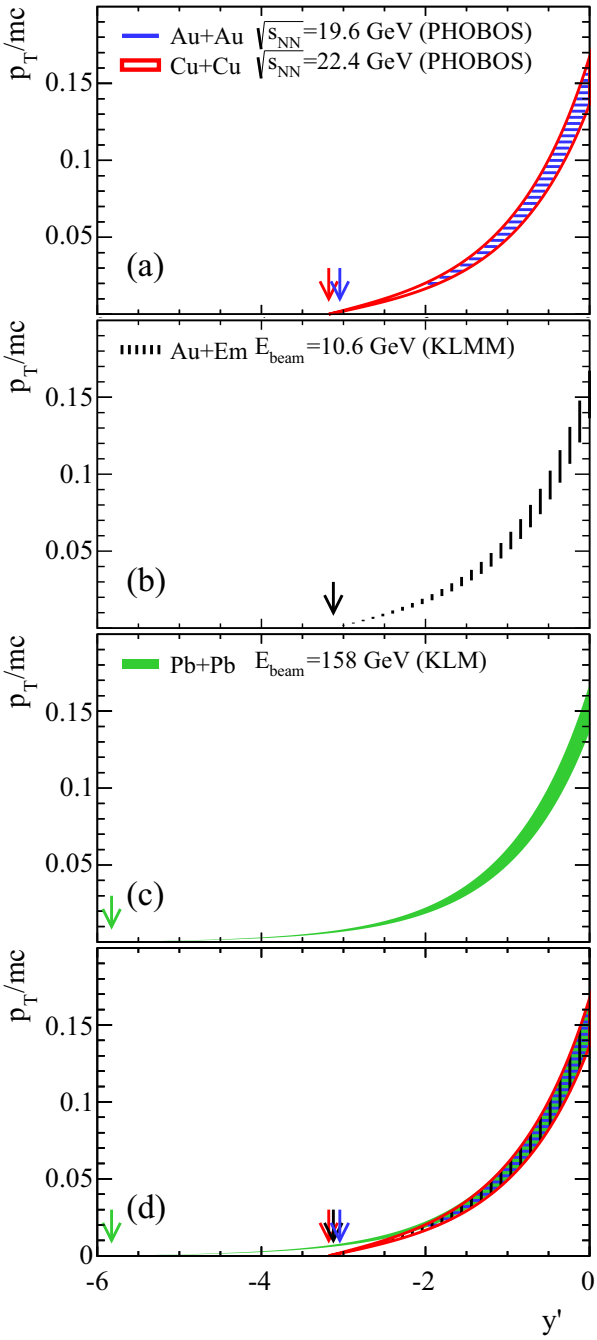

FIG. 17. p_T/m-y' acceptance for a fixed $1.8 < \eta' < 2.0$ window. The upper (lower) bound on each band corresponds to $\eta' = 1.8$ (2.0). The top three panels [(a)–(c)] show the acceptance for PHOBOS ($\sqrt{s_{NN}} = 19.6$ GeV, and 22.4 GeV), KLMM ($E_{\text{beam}} = 10.6$ GeV), and KLM ($E_{\text{beam}} = 158$ GeV), respectively. The lower panel (d) shows an overlay of all distributions. The arrows represent midrapidity ($y = 0$ and $\eta = 0$) at each energy. See text for discussion.

longitudinal scaling" region among data at different energies ($dN_{ch}/d\eta$ [16,20,21,24,25], and also for the first and second harmonic of the Fourier decomposition of the azimuthal angle distribution—known as v_1 [1] and v_2 [26], respectively). This is roughly confined to the $|\eta| > 2$ region, so, as shown, η' is ideally suited for this, second only to y' itself.

2. Limitations

As Fig. 17 suggests, there are limitations in this simplification. There are two important considerations in using η' rather than y'. The first is that the shape in $(y', p_T/m)$ space is non-intuitive and does *not* generally correspond to $\eta' = y'$ except when $p_T \gg m$. Therefore, generally interpreting an η' distribution as equivalent to y' can be seriously incorrect in certain cases. The second issue is that there can, in principle, be some contamination to high-η from particles with very low p_T and y that is not quite beam-energy independent. Usually the fact that these particles would have to come from very low p_T helps to suppress them since the $d^2N/dydp_T$ yields all go to 0 at $p_T = 0$. In particular, for the region of $\eta' > 0$, the midrapidity contribution is at *particularly* low p_T. For α particles in this work, the contamination from midrapidity can be expected to be negligible.

When comparing collider data to fixed target data, there is an extra consideration. For the positive side $\eta' = \eta - y_{\text{beam}}$, each η' bin contains contributions from all positive values of y. In the case of the collider kinematics this stops at midrapidity. In the case of fixed target kinematics this could, in principle, include contributions from particles near the target rapidity (which is 0). Therefore, some small contamination of α particles emitted at very low p_T from the target rather than from the Au beam could occur. Again, this is expected to be negligible, despite the extent in η, since it is at very low p_T and a very narrow window in p_T.

APPENDIX B: ESTIMATION OF dN/dp_T

The quantity dN/dp_T is known to be invariant under longitudinal boosts and may provide an additional check on scaling between data samples at different energies. The

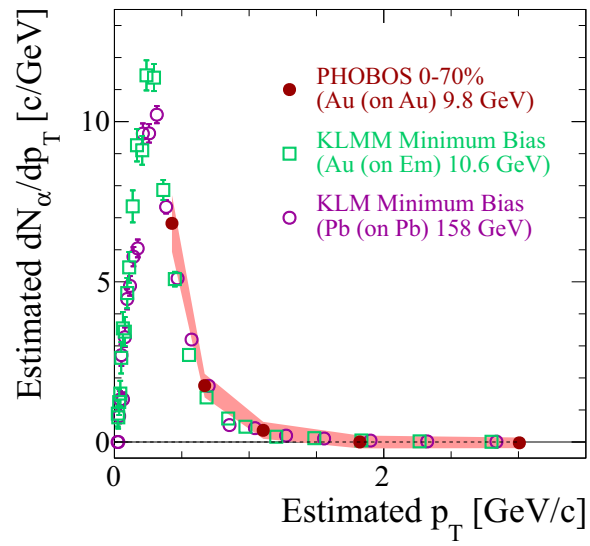

FIG. 18. Estimated dN/dp_T distribution for α fragments near beam rapidity for 0%–70% central Au+Au collisions at $\sqrt{s_{NN}} = 19.6$ GeV. Estimation procedure is described in the text. For comparison, Au+Em ($\sqrt{s_{NN}} = 4.6$ GeV) [4] and Pb+Pb ($\sqrt{s_{NN}} = 17.2$ GeV) [7] collisions are shown, using the same estimation method.

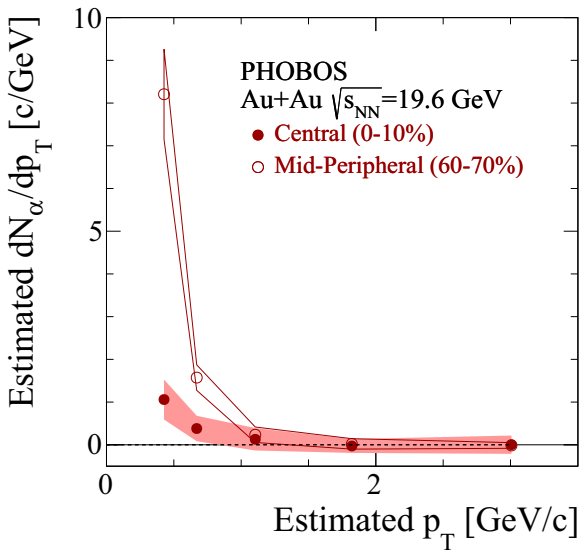

FIG. 19. Estimated dN/dp_T distribution for α fragments near beam rapidity for Au+Au collisions at $\sqrt{s_{NN}} = 19.6$ GeV. Estimation procedure is described in the text. The open and closed symbols represent central (0%–10%) and midperipheral (60%–70%) collisions, respectively.

measurement of p_T is not possible at forward pseudorapidity in PHOBOS, so an estimate is needed. It is assumed that the longitudinal momentum of the spectator nucleons does not change during the collision. Given this assumption, one can calculate the transverse momentum as

$$p_T = \frac{m\sinh(y_{\text{beam}})}{\sinh(\eta)}, \tag{B1}$$

where m is the mass of the particle of interest (α). Differentiating Eq. (B1) yields the Jacobian needed to transform $dN/d\eta \rightarrow dN/dp_T$:

$$\frac{d\eta}{dp_T} = \frac{d\eta'}{dp_T} = -\frac{\tanh(\eta)}{p_T}. \tag{B2}$$

Using these relations [Eqs. (B1) and (B2)], one can transform $dN/d\eta$ as a function of η into dN/dp_T as a function of p_T. As a reminder, this is an estimate of both quantities and is not a precise measurement. Figure 18 shows a comparison of the estimated dN/dp_T versus p_T for 0%–70% central Au+Au collisions at $\sqrt{s_{NN}} = 19.6$ GeV. For comparison, the same technique is used to transform the data from Au+Em ($\sqrt{s_{NN}} = 4.6$ GeV) [4] and Pb+Pb ($\sqrt{s_{NN}} = 17.2$ GeV) [7] collisions (i.e., from the data shown in Fig. 9). The data agree well within the uncertainties described above. Figure 19 shows a comparison between central (closed symbols) and midperipheral (open) Au+Au collisions. The Cu+Cu data are not shown as the expected difference in yield between Au (197) fragments and Cu (63) fragments is large because of the difference in mass—whereas the difference between Au (197) and Pb (208) should be negligible.

TABLE I. N_{part} values determined from a Glauber model calculation for Au+Au ($\sqrt{s_{NN}} = 19.6$ GeV) and Cu+Cu ($\sqrt{s_{NN}} = 22.4$ GeV) collisions. Uncertainties are 90% C.L. systematic.

Centrality bin (%)	Number of participants Au+Au	Cu+Cu
0–10	316.3 ± 9.9	93.8 ± 3.0
10–20	226.5 ± 8.0	68.5 ± 3.0
20–30	156.5 ± 7.0	48.5 ± 3.0
30–40	106.0 ± 7.0	33.5 ± 3.0
40–50	66.0 ± 4.7	22.0 ± 3.0
50–60	39.5 ± 3.0	14.3 ± 3.0
60–70	21.3 ± 3.0	–

APPENDIX C: TABLES OF DATA

Table I shows the N_{part} values determined from a Glauber model calculation for Au+Au ($\sqrt{s_{NN}} = 19.6$ GeV) and Cu+Cu ($\sqrt{s_{NN}} = 22.4$ GeV) collisions.

Tables II–VII contain the corrected $dN_{\text{particle}}/d\eta$ yields as function of collision centrality for Au+Au ($\sqrt{s_{NN}} = 19.6$ GeV) and Cu+Cu ($\sqrt{s_{NN}} = 22.4$ GeV) collisions, respectively. Note that for clarity some values are scaled up by powers of 10.

TABLE II. $dN_\alpha/d\eta$ measured in Au+Au collisions at $\sqrt{s_{NN}} = 19.6$ GeV. Uncertainties are 1-σ statistical and 90% C.L. systematic.

Centrality	Yield				
bin (%)	$3.0 < \lvert\eta\rvert < 3.5$	$3.5 < \lvert\eta\rvert < 4.0$	$4.0 < \lvert\eta\rvert < 4.5$	$4.5 < \lvert\eta\rvert < 5.0$	$5.0 < \lvert\eta\rvert < 5.4$
0–10	0.01 ± 0.03 ± 0.65	−0.05 ± 0.02 ± 0.30	0.14 ± 0.01 ± 0.29	0.26 ± 0.01 ± 0.20	0.45 ± 0.02 ± 0.20
10–20	−0.00 ± 0.02 ± 0.46	−0.24 ± 0.02 ± 0.86	0.41 ± 0.02 ± 0.36	0.84 ± 0.02 ± 0.20	1.67 ± 0.03 ± 0.20
20–30	−0.08 ± 0.02 ± 0.55	0.09 ± 0.01 ± 0.33	0.52 ± 0.02 ± 0.30	1.38 ± 0.02 ± 0.20	2.95 ± 0.04 ± 0.27
30-40	−0.25 ± 0.02 ± 0.64	0.12 ± 0.01 ± 0.33	0.57 ± 0.02 ± 0.34	1.64 ± 0.02 ± 0.28	3.82 ± 0.04 ± 0.56
40–50	−0.22 ± 0.02 ± 0.70	0.04 ± 0.01 ± 0.33	0.51 ± 0.02 ± 0.29	1.68 ± 0.02 ± 0.43	4.06 ± 0.04 ± 0.45
50–60	0.05 ± 0.01 ± 0.33	0.01 ± 0.01 ± 0.20	0.40 ± 0.01 ± 0.28	1.40 ± 0.02 ± 0.22	3.95 ± 0.04 ± 0.52
60–70	−0.05 ± 0.01 ± 0.20	0.04 ± 0.01 ± 0.22	0.26 ± 0.01 ± 0.20	1.05 ± 0.02 ± 0.20	3.51 ± 0.04 ± 0.45

TABLE III. $dN_{Li}/d\eta$ measured in Au+Au collisions at $\sqrt{s_{NN}} = 19.6$ GeV. Uncertainties are 1-σ statistical and 90% C.L. systematic. Yields are scaled up by a factor of 10 for clarity.

Centrality	Yield × 10				
bin (%)	$3.0 < \|\eta\| < 3.5$	$3.5 < \|\eta\| < 4.0$	$4.0 < \|\eta\| < 4.5$	$4.5 < \|\eta\| < 5.0$	$5.0 < \|\eta\| < 5.4$
0–10	$0.41 \pm 0.07 \pm 0.47$	$0.01 \pm 0.05 \pm 0.34$	$0.05 \pm 0.03 \pm 0.22$	$0.03 \pm 0.03 \pm 0.20$	$0.08 \pm 0.04 \pm 0.51$
10–20	$0.06 \pm 0.07 \pm 0.48$	$-0.19 \pm 0.05 \pm 0.76$	$0.08 \pm 0.04 \pm 0.29$	$0.17 \pm 0.04 \pm 0.20$	$0.66 \pm 0.07 \pm 0.20$
20–30	$0.12 \pm 0.06 \pm 0.36$	$0.09 \pm 0.04 \pm 0.36$	$0.13 \pm 0.04 \pm 0.33$	$0.26 \pm 0.04 \pm 0.20$	$1.23 \pm 0.09 \pm 0.20$
30–40	$-0.05 \pm 0.06 \pm 0.43$	$0.13 \pm 0.04 \pm 0.24$	$0.02 \pm 0.04 \pm 0.30$	$0.59 \pm 0.05 \pm 0.26$	$1.88 \pm 0.11 \pm 0.63$
40–50	$-0.09 \pm 0.05 \pm 0.51$	$0.01 \pm 0.03 \pm 0.27$	$0.25 \pm 0.04 \pm 0.35$	$0.66 \pm 0.05 \pm 0.37$	$1.88 \pm 0.11 \pm 0.20$
50–60	$0.03 \pm 0.04 \pm 0.25$	$-0.02 \pm 0.03 \pm 0.21$	$0.14 \pm 0.03 \pm 0.20$	$0.41 \pm 0.05 \pm 0.20$	$1.71 \pm 0.11 \pm 0.25$
60–70	$0.04 \pm 0.03 \pm 0.20$	$0.08 \pm 0.02 \pm 0.28$	$0.02 \pm 0.03 \pm 0.20$	$0.28 \pm 0.04 \pm 0.20$	$1.19 \pm 0.10 \pm 0.30$

TABLE IV. $dN_{Be}/d\eta$ measured in Au+Au collisions at $\sqrt{s_{NN}} = 19.6$ GeV. Uncertainties are 1-σ statistical and 90% C.L. systematic. Yields are scaled up by a factor of 100 for clarity.

Centrality	Yield × 100				
bin (%)	$3.0 < \|\eta\| < 3.5$	$3.5 < \|\eta\| < 4.0$	$4.0 < \|\eta\| < 4.5$	$4.5 < \|\eta\| < 5.0$	$5.0 < \|\eta\| < 5.4$
0–10	$0.09 \pm 0.45 \pm 0.73$	$-0.43 \pm 0.30 \pm 1.14$	$-0.24 \pm 0.22 \pm 0.59$	$-0.31 \pm 0.14 \pm 0.60$	$0.26 \pm 0.22 \pm 0.41$
10–20	$0.02 \pm 0.41 \pm 0.65$	$-0.53 \pm 0.30 \pm 1.58$	$-0.38 \pm 0.25 \pm 1.02$	$0.26 \pm 0.21 \pm 0.38$	$1.17 \pm 0.36 \pm 0.96$
20–30	$-0.37 \pm 0.37 \pm 0.95$	$-0.52 \pm 0.25 \pm 1.18$	$0.18 \pm 0.26 \pm 0.63$	$0.58 \pm 0.27 \pm 0.43$	$2.09 \pm 0.49 \pm 1.24$
30–40	$-0.43 \pm 0.36 \pm 1.46$	$0.30 \pm 0.25 \pm 0.48$	$0.36 \pm 0.25 \pm 1.07$	$-0.12 \pm 0.24 \pm 0.43$	$2.84 \pm 0.58 \pm 0.73$
40–50	$-0.47 \pm 0.29 \pm 1.22$	$-0.25 \pm 0.21 \pm 0.73$	$-0.46 \pm 0.22 \pm 0.83$	$0.55 \pm 0.26 \pm 0.52$	$3.13 \pm 0.61 \pm 0.66$
50–60	$-0.14 \pm 0.23 \pm 0.59$	$0.21 \pm 0.19 \pm 0.34$	$0.13 \pm 0.23 \pm 0.37$	$0.53 \pm 0.26 \pm 0.47$	$2.29 \pm 0.55 \pm 2.32$
60–70	$-0.24 \pm 0.17 \pm 0.42$	$0.03 \pm 0.15 \pm 0.26$	$-0.20 \pm 0.18 \pm 0.66$	$0.24 \pm 0.23 \pm 0.47$	$2.04 \pm 0.51 \pm 1.32$

TABLE V. $dN_B/d\eta$ measured in Au+Au collisions at $\sqrt{s_{NN}} = 19.6$ GeV. Uncertainties are 1-σ statistical and 90% C.L. systematic. Yields are scaled up by a factor of 100 for clarity.

Centrality	Yield × 100				
bin (%)	$3.0 < \|\eta\| < 3.5$	$3.5 < \|\eta\| < 4.0$	$4.0 < \|\eta\| < 4.5$	$4.5 < \|\eta\| < 5.0$	$5.0 < \|\eta\| < 5.4$
0–10	$-0.09 \pm 0.41 \pm 1.15$	$-0.19 \pm 0.29 \pm 0.75$	$-0.04 \pm 0.23 \pm 0.84$	$-0.21 \pm 0.16 \pm 0.60$	$-0.29 \pm 0.10 \pm 0.63$
10–20	$0.17 \pm 0.40 \pm 0.80$	$0.70 \pm 0.35 \pm 1.04$	$0.41 \pm 0.28 \pm 1.03$	$0.06 \pm 0.18 \pm 0.43$	$0.32 \pm 0.29 \pm 0.37$
20–30	$-0.45 \pm 0.36 \pm 1.01$	$-0.45 \pm 0.24 \pm 1.34$	$-0.39 \pm 0.23 \pm 1.43$	$-0.23 \pm 0.22 \pm 0.43$	$1.60 \pm 0.46 \pm 0.94$
30–40	$0.38 \pm 0.40 \pm 0.95$	$0.17 \pm 0.26 \pm 0.76$	$0.16 \pm 0.25 \pm 1.01$	$0.01 \pm 0.24 \pm 0.54$	$2.31 \pm 0.56 \pm 1.03$
40–50	$0.45 \pm 0.31 \pm 0.95$	$0.05 \pm 0.22 \pm 0.82$	$-0.37 \pm 0.22 \pm 1.30$	$0.05 \pm 0.23 \pm 0.78$	$2.01 \pm 0.56 \pm 0.86$
50–60	$-0.11 \pm 0.22 \pm 0.89$	$0.07 \pm 0.18 \pm 0.50$	$-0.02 \pm 0.22 \pm 0.58$	$0.34 \pm 0.25 \pm 0.50$	$3.36 \pm 0.57 \pm 1.29$
60–70	$-0.29 \pm 0.15 \pm 0.75$	$-0.04 \pm 0.15 \pm 0.68$	$-0.11 \pm 0.18 \pm 0.47$	$0.03 \pm 0.21 \pm 0.38$	$1.71 \pm 0.48 \pm 0.46$

TABLE VI. $dN_\alpha/d\eta$ measured in Cu+Cu collisions at $\sqrt{s_{NN}} = 22.4$ GeV. Uncertainties are 1-σ statistical and 90% C.L. systematic. Yields are scaled up by a factor of 10 for clarity.

Centrality	Yield × 10				
bin (%)	$3.0 < \|\eta\| < 3.5$	$3.5 < \|\eta\| < 4.0$	$4.0 < \|\eta\| < 4.5$	$4.5 < \|\eta\| < 5.0$	$5.0 < \|\eta\| < 5.4$
0–10	$-0.15 \pm 0.16 \pm 0.50$	$-0.16 \pm 0.09 \pm 0.56$	$0.28 \pm 0.04 \pm 0.50$	$0.87 \pm 0.07 \pm 0.50$	$1.94 \pm 0.07 \pm 0.50$
10–20	$0.21 \pm 0.08 \pm 0.50$	$0.21 \pm 0.14 \pm 0.50$	$0.63 \pm 0.06 \pm 0.50$	$2.04 \pm 0.09 \pm 0.50$	$5.06 \pm 0.09 \pm 0.79$
20–30	$0.11 \pm 0.09 \pm 0.50$	$0.20 \pm 0.08 \pm 0.50$	$0.77 \pm 0.06 \pm 0.50$	$2.62 \pm 0.10 \pm 0.55$	$7.35 \pm 0.12 \pm 1.34$
30–40	$0.08 \pm 0.08 \pm 0.50$	$0.09 \pm 0.07 \pm 0.50$	$0.75 \pm 0.06 \pm 0.50$	$2.80 \pm 0.07 \pm 0.50$	$8.09 \pm 0.12 \pm 1.37$
40–50	$0.13 \pm 0.10 \pm 0.50$	$0.11 \pm 0.06 \pm 0.50$	$0.66 \pm 0.05 \pm 0.50$	$2.47 \pm 0.06 \pm 0.50$	$7.23 \pm 0.11 \pm 1.19$
50–60	$0.08 \pm 0.05 \pm 0.50$	$0.12 \pm 0.06 \pm 0.50$	$0.45 \pm 0.04 \pm 0.50$	$1.95 \pm 0.05 \pm 0.50$	$5.99 \pm 0.10 \pm 1.04$

TABLE VII. $dN_{Li}/d\eta$ measured in Cu+Cu collisions at $\sqrt{s_{NN}} = 22.4$ GeV. Uncertainties are 1-σ statistical and 90% C.L. systematic. Yields are scaled up by a factor of 100 for clarity.

Centrality	Yield × 100				
bin (%)	$3.0 < \|\eta\| < 3.5$	$3.5 < \|\eta\| < 4.0$	$4.0 < \|\eta\| < 4.5$	$4.5 < \|\eta\| < 5.0$	$5.0 < \|\eta\| < 5.4$
0–10	$0.61 \pm 0.40 \pm 2.40$	$0.41 \pm 0.37 \pm 0.71$	$0.25 \pm 0.09 \pm 0.53$	$0.37 \pm 0.08 \pm 0.40$	$0.03 \pm 0.12 \pm 0.42$
10–20	$0.05 \pm 0.22 \pm 2.15$	$0.12 \pm 0.22 \pm 0.58$	$0.39 \pm 0.10 \pm 0.80$	$0.46 \pm 0.10 \pm 0.54$	$0.40 \pm 0.17 \pm 0.40$
20–30	$0.45 \pm 0.18 \pm 1.03$	$0.14 \pm 0.20 \pm 0.77$	$0.19 \pm 0.09 \pm 0.61$	$0.13 \pm 0.12 \pm 0.58$	$0.96 \pm 0.23 \pm 0.49$
30–40	$0.44 \pm 0.18 \pm 1.25$	$0.28 \pm 0.18 \pm 0.68$	$0.24 \pm 0.09 \pm 0.40$	$0.19 \pm 0.08 \pm 0.66$	$1.23 \pm 0.31 \pm 0.68$
40–50	$0.28 \pm 0.11 \pm 0.80$	$0.26 \pm 0.15 \pm 0.41$	$0.14 \pm 0.07 \pm 0.40$	$0.17 \pm 0.08 \pm 0.40$	$1.22 \pm 0.22 \pm 0.40$
50–60	$0.20 \pm 0.10 \pm 0.65$	$0.20 \pm 0.10 \pm 0.40$	$0.03 \pm 0.07 \pm 0.40$	$0.10 \pm 0.07 \pm 0.40$	$0.90 \pm 0.24 \pm 0.41$

[1] B. B. Back *et al.* (PHOBOS Collaboration), Phys. Rev. Lett. **97**, 012301 (2006).
[2] M. I. Adamovich *et al.* (EMU-01 Collaboration), Phys. Rev. C **40**, 66 (1989).
[3] G. Singh and P. L. Jain, Z. Phys. A **348**, 99 (1994).
[4] M. L. Cherry *et al.* (KLMM Collaboration), Phys. Rev. C **52**, 2652 (1995).
[5] A. Schuettauf *et al.* (ALADIN Collaboration), Nucl. Phys. A **607**, 457 (1996).
[6] M. L. Cherry *et al.* (KLMM Collaboration), Z. Phys. C **73**, 449 (1997).
[7] M. L. Cherry *et al.* (KLM Collaboration), Acta Phys. Polon. B **29**, 2155 (1998).
[8] J. Barrette *et al.* (E877 Collaboration), Phys. Rev. C **61**, 044906 (2000).
[9] A. Dabrowska, B. Wosiek, and C. J. Waddington, Acta Phys. Polon. B **31**, 725 (2000).
[10] B. B. Back *et al.* (PHOBOS Collaboration), Nucl. Instrum. Methods Phys. Res. A **499**, 603 (2003).
[11] C. Adler*el al.*, Nucl. Instrum. Methods Phys. Res. A **470**, 488 (2001).
[12] R. Bindel *et al.*, Nucl. Instrum. Methods Phys. Res. A **474**, 38 (2001).
[13] E. Garcia *et al.*, Nucl. Instrum. Methods Phys. Res. A **570**, 536 (2007).
[14] B. B. Back *et al.* (PHOBOS Collaboration), Phys. Rev. C **70**, 021902(R) (2004).
[15] B. Alver, M. Baker, C. Loizides, and P. Steinberg, arXiv:0805.4411v1, and references therein.
[16] B. B. Back *et al.* (PHOBOS Collaboration), Phys. Rev. Lett. **91**, 052303 (2003).
[17] M. Gyulassy and X. N. Wang, Comput. Phys. Commun. **83**, 307 (1994), version 1.35 is used.
[18] GEANT 3.21, CERN Program Library, Geneva.
[19] B. B. Back *et al.* (PHOBOS Collaboration), Phys. Rev. C **65**, 031901(R) (2002).
[20] B. Alver *et al.* (PHOBOS Collaboration), Phys. Rev. C **83**, 024913 (2011).
[21] B. Alver *et al.* (PHOBOS Collaboration), Phys. Rev. Lett. **102**, 142301 (2009).
[22] B. B. Back *et al.* (PHOBOS Collaboration), Nucl. Phys. A **757**, 28 (2005).
[23] J. Beringer *et al.* (Particle Data Group), Phys. Rev. D **86**, 010001 (2012), see Sec. 43.5.
[24] B. B. Back *et al.* (PHOBOS Collaboration), Phys. Rev. C **72**, 031901(R) (2005).
[25] B. B. Back *et al.* (PHOBOS Collaboration), Phys. Rev. C **74**, 021901(R) (2006).
[26] B. Alver *et al.* (PHOBOS Collaboration), Phys. Rev. Lett. **98**, 242302 (2007).